Bioactive Materials 15 (2022) 482–494

Contents lists available at ScienceDirect

Bioactive Materials

journal homepage: www.keaipublishing.com/en/journals/bioactive-materials

# Bioinspired *Andrias davidianus*-Derived wound dressings for localized drug-elution

Xiang Liu [a,1], Xiang Mao [b,1], Guo Ye [c,1], Menghong Wang [a], Ke Xue [d,g], Yan Zhang [a], Hongmei Zhang [a], Xiaoqiao Ning [a], Man Zhao [e], Jinlin Song [a,*], Yu Shrike Zhang [f,**], Ximu Zhang [a,***]

[a] Chongqing Key Laboratory of Oral Disease and Biomedical Sciences and Chongqing Municipal Key Laboratory of Oral Biomedical Engineering of Higher Education and Stomatological Hospital, Chongqing Medical University, Chongqing, 401174, China
[b] State Key Laboratory of Ultrasound in Medicine and Engineering and Chongqing Key Laboratory of Biomedical Engineering, College of Biomedical Engineering, Chongqing Medical University, Chongqing, 400016, China
[c] Department of Stomatology, The Third Affiliated Hospital, Chongqing Medical University, Chongqing, 401120, China
[d] Department of Plastic and Reconstructive Surgery, Shanghai Ninth People's Hospital, Shanghai Jiao Tong University School of Medicine, 639 Zhi Zao Ju Rd, Shanghai, 200011, China
[e] Department of Pharmacy, The 958th Hospital of PLA, Chongqing, 404100, China
[f] Division of Engineering in Medicine, Department of Medicine, Brigham and Women's Hospital, Harvard Medical School, Cambridge, MA, 02139, USA
[g] Department of Plastic and reconstructive surgery, Hainan Western Central Hospital, HaiNan, 571700, China

ARTICLE INFO

*Keywords:*
*Andrias davidianus*
Hydrogel
Drug loading
Controlled drug delivery
Stem cell recruitment
Wound healing

ABSTRACT

Local drug delivery has received increasing attention in recent years. However, the therapeutic efficacy of local delivery of drugs is still limited under certain scenarios, such as in the oral cavity or in wound beds after resection of tumors. In this study, we introduce a bioinspired adhesive hydrogel derived from the skin secretions of *Andrias davidianus* (SSAD) as a wound dressing for localized drug elution. The hydrogel was loaded with aminoguanidine or doxorubicin, and its controlled drug release and healing-promoting properties were verified in a diabetic rat palatal mucosal defect model and a C57BL/6 mouse melanoma-bearing model, respectively. The results showed that SSAD hydrogels with different pore sizes could release drugs in a controllable manner and accelerate wound healing. Transcriptome analyses of the palatal mucosa suggested that SSAD could significantly upregulate pathways linked to cell adhesion and extracellular matrix deposition and had the ability to recruit keratinocyte stem cells to defect sites. Taken together, these findings indicate that property-controllable SSAD hydrogels could be a promising biofunctional wound dressing for local drug delivery and promotion of wound healing.

## 1. Introduction

Traditional delivery methods based on systemic administration can lead to side effects and low bioavailability [1]. As such, local administration has received increasing attention in recent years because it can improve local drug bioavailability and reduce drug-induced systemic toxicity [2]. However, this approach is still limited by certain shortcomings, such as the complex wound sites in the oral cavity or the wound beds after tumor resection.

Periodontitis and diabetes mellitus are highly related common chronic diseases. Under a hyperglycemic environment caused by diabetes, advanced glycation end-products (AGEs) may largely accumulate in periodontal tissues [3], which subsequently induces cell apoptosis, reduces the proliferation and migration of cells related to wound healing [4,5], and inhibits stem cell differentiation [6,7], eventually impairing the wound-healing process. Although systemic administration of aminoguanidine (AG, an AGE-inhibitor) has been proven to accelerate palatal wound healing in diabetic rats after free gingival grafting (FGG)

Peer review under responsibility of KeAi Communications Co., Ltd.
* Corresponding author.
** Corresponding author.
*** Corresponding author.
*E-mail addresses:* songjinlin@hospital.cqmu.edu.cn (J. Song), yszhang@research.bwh.harvard.edu (Y.S. Zhang), zhangximu@hospital.cqmu.edu.cn (X. Zhang).
[1] Co-first authors.

https://doi.org/10.1016/j.bioactmat.2021.11.030
Received 11 April 2021; Received in revised form 20 October 2021; Accepted 22 November 2021
Available online 14 January 2022

[8], some safety concerns related to the use of high concentrations of AG have also been reported [9–11]. Moreover, the moist condition of the oral cavity and constant mastication stop drugs from being retained locally [12].

On the other hand, malignant melanoma is considered to be one of the most aggressive and highly metastatic skin tumors [13], and surgical resection is still the most commonly used treatment in the clinic [14]. Potential residual melanoma cells after surgical resection can easily lead to cancer recurrence [14]. Therefore, local resection combined with systemic chemotherapy is a common treatment approach. Nevertheless, the nonspecific distribution of chemotherapy drugs and fluctuating blood concentrations always result in serious side effects and place a significant burden on patients [15]. Consequently, topical chemotherapy is increasingly being used to minimize drug exposure to healthy tissues while reducing the risk of local recurrence. However, most chemotherapy drugs, such as doxorubicin (DOX), have relatively poor specificity and cannot distinguish between normal and cancer cells [16].

Ideally, a local drug delivery system for wound healing should be cost-effective, safe and possess multiple functions, such as controlled release, local retention, biodegradability, and pro-healing abilities. To overcome the above-mentioned deficiencies, as we recently reported, a bioadhesive derived from the skin secretion of *Andrias davidianus* (SSAD) exhibits strong tissue adhesion and is readily biodegradable *in vivo*, which could reduce the secondary damage inflicted during dressing changes [17,56]. This bioadhesive could be modified and used as a drug-loaded wound dressing to promote wound healing. However, SSAD-based drug delivery systems remain to be investigated for their hypothesized strong potential in various translational applications.

In this study, we prepared a series of SSAD hydrogels with different properties by controlling the corresponding SSAD powder particle sizes (20, 60, and 200 meshes) and subsequently loaded them with different drugs (AG or DOX). First, we verified the ability of SSAD to sustain drug release *in vitro*. Then, animal experiments using a palatal mucosal defect model or a melanoma-bearing model were conducted to fully verify the dual functions of SSAD for simultaneous local delivery of drugs and promotion of wound healing *in vivo*. SSAD application combined with controlled release of pharmaceutical agents and the mechanism by which it promotes regeneration were systematically investigated (Fig. 1).

## 2. Results and discussion

### 2.1. Structural characterization and drug release properties of SSAD

As shown in Fig. 2a, SSAD powders with different mesh sizes were readily obtained, and these powders resulted in hydrogels with different porous properties. The formed hydrogels suggested that the SSAD particle size and the associated variations in the hydration process directly influenced the pore sizes of the resulting hydrogels [55]. After mixing of the SSAD particles with water, they hydrate and swell to form a hydrogel with a porous structure induced by hydrogen bonding and S–S bonds between amino acid residues of SSAD proteins [17]. The pores on the hydrogel surfaces were circular and interconnected, which could be the result of two factors: the micropores were formed from the SSAD powder hydration, and the macropores were determined by the SSAD particle size. This observation confirmed that a denser mesh was related to smaller pores and suggested that the accompanying hydrogel network might be more stable [17].

Fourier-transform infrared (FT-IR) spectra further illustrated the successful loading of AG or DOX molecules within SSAD, as shown in Fig. 2b. For pure AG or DOX molecules, absorption bands attributable to the stretching vibrations of the main alkyl chains could be observed at 3,440 $cm^{-1}$ and 3,326 $cm^{-1}$, respectively (Fig. 2b i). The stretch vibration peak of N–H appeared at 3,435 $cm^{-1}$ before SSAD loading with drugs (Fig. 2b ii and iii). However, there were two peaks (3,274 $cm^{-1}$ or 3,500 $cm^{-1}$) present after integration with either AG or DOX, as revealed in Fig. 2b ii and iii, respectively. Given the absence of reactive chemical groups in the drug molecules, their loading within the SSAD hydrogels could mainly be attributed to physical entrapment or adsorption through various noncovalent interactions.

To evaluate the drug release properties of the SSAD hydrogels made from powders of different particle sizes, 20-, 60-, and 200-mesh hydrogels were constructed. AG (Mw: 111.55) and DOX (Mw: 543.52) were chosen as model drugs for loading into the SSAD hydrogels. During the assessment period (24 h). The cumulative AG released from the 20-, 60-, and 200-mesh SSAD hydrogels was 64%, 56%, and 50%, respectively (Fig. 2c). The cumulative DOX released from the 20-, 60-, and 200-mesh SSAD hydrogels was 73%, 70%, and 51%, respectively (Fig. 2d). With an increase in the particle size of the SSAD powder, the drug

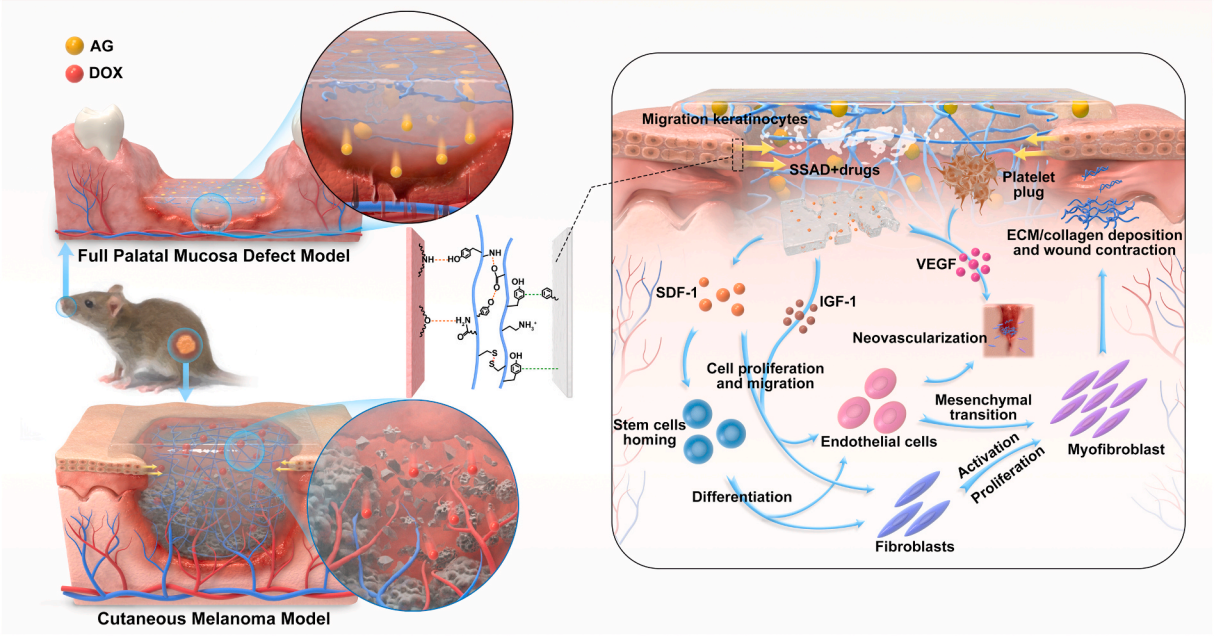


**Fig. 1.** Schematic diagram showing the two animal models used in this study and the possible mechanism by which the drug-loaded SSAD hydrogel promotes wound healing.

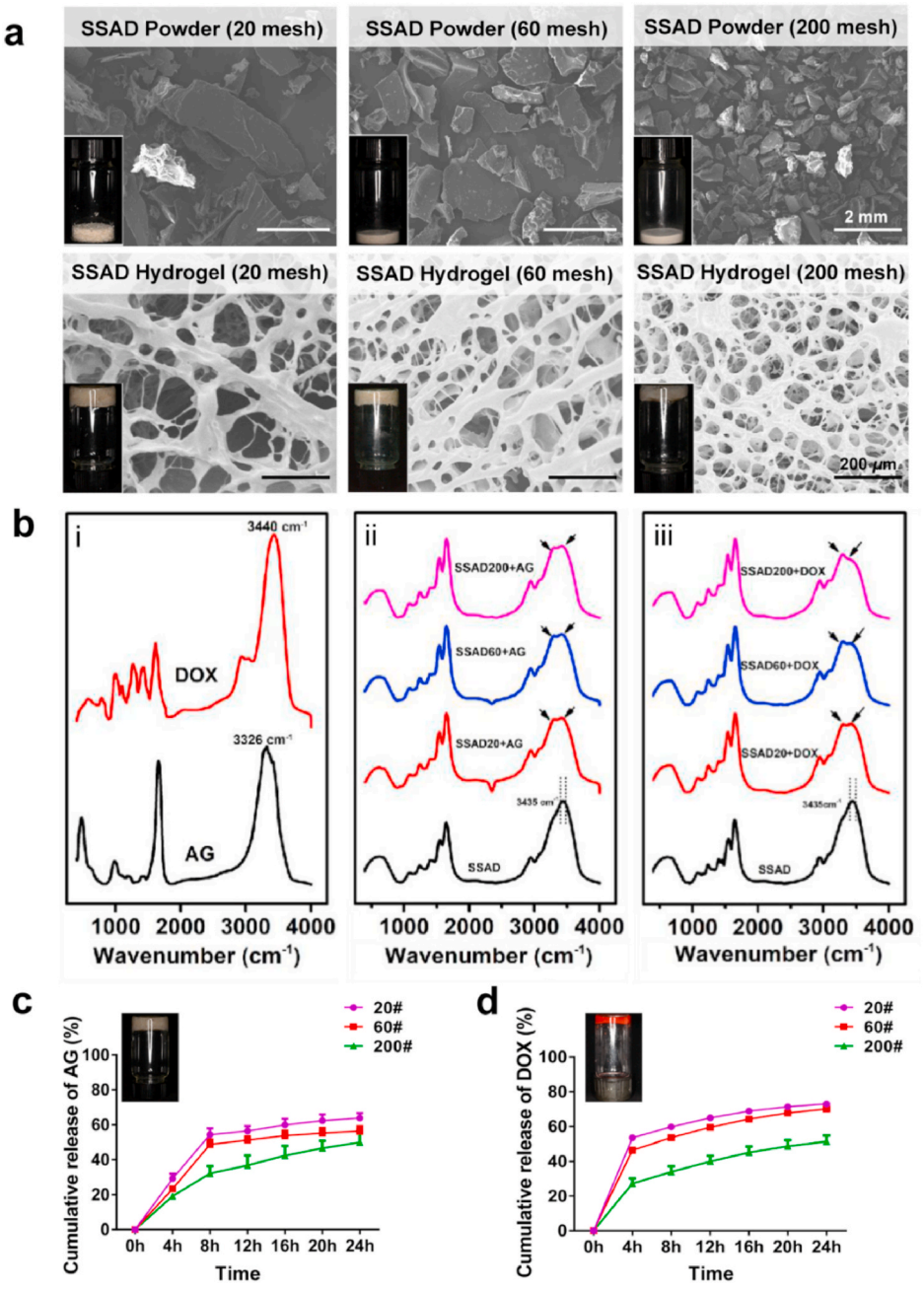


**Fig. 2.** Structural characterizations and sustained drug release properties of SSAD. (a) SEM images showing the sizes of the 20-, 60-, and 200-mesh SSAD powders and the porous structures of the corresponding formed hydrogels. (b) FR-IR characterization of i) AG and DOX, ii) AG loaded in SSAD hydrogels of different pore sizes (20, 60, and 200 meshes), and iii) DOX with different SSAD hydrogels of different pore sizes (20, 60, and 200 meshes). (c, d) Cumulative release profiles of (c) AG and (d) DOX in SSAD hydrogels of different pore sizes (20, 60, and 200 meshes).

release rate from the corresponding SSAD hydrogel increased. In addition, to analyze *in vitro* degradation behavior of the SSAD hydrogels, they were immersed in phosphate-buffered saline (PBS) or human saliva at 37 °C for 24 h. The degradation behaviors were measured at different time intervals (Fig. S1). The SSAD hydrogels degraded gradually in both PBS and saliva. During the earlier 8 h, the mass of the hydrogels (20, 60, and 200 meshes) were reduced quickly; after 8 h, all the hydrogels (20, 60, and 200 meshes) had degraded gradually and reached an equilibrium state at 36 h. These results showed that the hydrogel degradation rate increased with the SSAD particle size and consequently, the larger pore size of the resulting hydrogel during degradation.

### 2.2. *In vitro cytological studies*

#### 2.2.1. *Cell proliferation induced by SSAD*

Cell Counting Kit-8 (CCK-8) assays were used to evaluate the biocompatibility of SSAD with L929 fibroblasts and human umbilical vein endothelial cells (HUVECs), both of which play important roles in skin and mucosal regeneration [19]. In our preliminary experiment (Fig. S2), we had evaluated the cytotoxicity of SSAD towards L929 cells and HUVECs with Dulbecco's modified Eagle's medium (DMEM) containing a series of SSAD concentrations (from 5 to 0.005 mg/mL). Among the different concentrations, 0.1 mg/mL of SSAD seemed to be a good intermediate concentration that promoted cell proliferation, and was chosen for subsequent cell experiments.

#### 2.2.2. *Cell migration induced by SSAD*

Scratch (Fig. 3a) and Transwell migration (Fig. 3b) assays were used to verify the effects of SSAD on the migration of L929 cells and HUVECs *in vitro*. Compared to the control group, SSAD-conditioned medium significantly promoted the lateral migration of L929 cells (1.5-fold of the control group) and HUVECs (1.7-fold of the control group) (Fig. 3c). Compared to the control group, SSAD-conditioned medium also significantly promoted the transmembrane migration of L929 cells (2.1-fold of

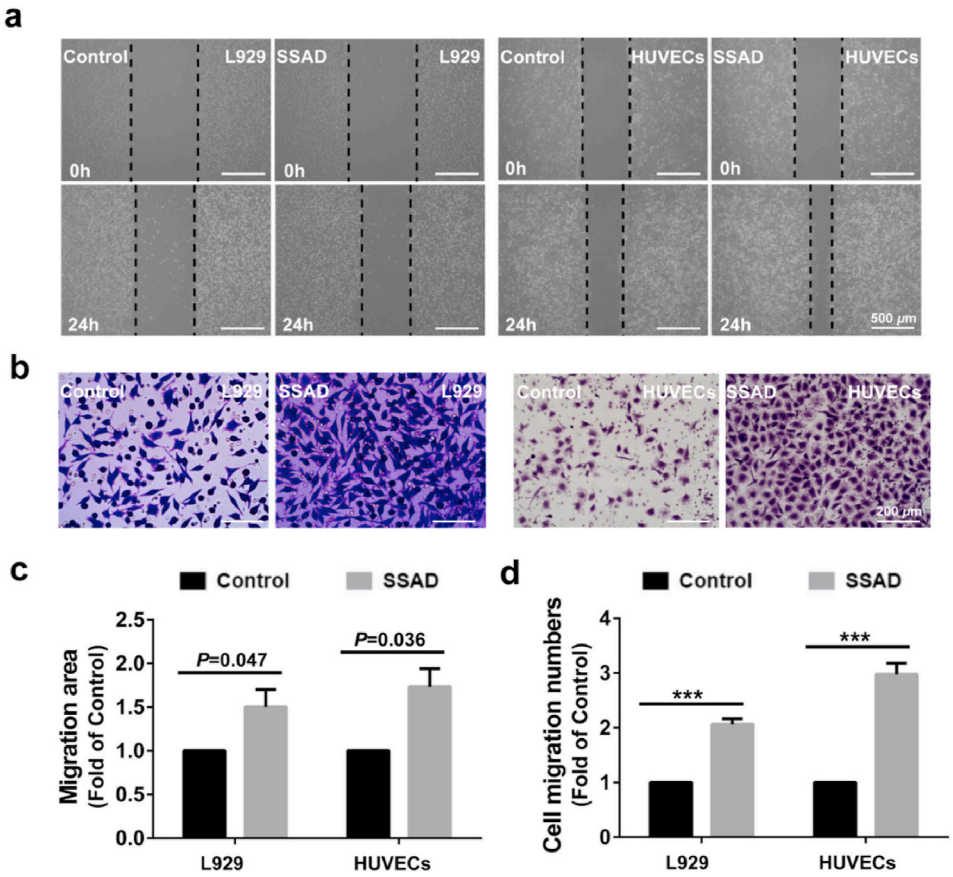


**Fig. 3.** Cell migration induced by SSAD. (a) Scratch assay of L929 cells and HUVECs cultured with or without SSAD. (b) The migratory abilities of L929 cells and HUVECs treated with or without SSAD were further confirmed by Transwell assays. (c, d) Quantitative analyses of (c) the relative migration areas in the scratch assay and (d) the number of cells that migrated from the top chamber to the bottom chamber in the Transwell assay. (*$P < 0.05$, **$P < 0.01$, ***$P < 0.001$).

the control group) and HUVECs (3.0-fold of the control group) (Fig. 3d). Since cell migration is a critical step in wound healing [20], the above results indicate that SSAD can dramatically increase the migration of relevant cell types, potentially also in wound areas.

As is well-recognized, the expressions of a number of growth factors may be beneficial in the process of wound healing [21]. Our bioassay results showed that SSAD contained a collection of growth factors, such as vascular endothelial growth factor (VEGF), insulin-like growth factor 1 (IGF-1), and stromal cell-derived factor-1 (SDF-1), among others (Table S1). According to the content of each growth factor SSAD contains, we chose IGF-1 and SDF-1, which are the two most abundant ones in SSAD. SSAD exhibited a better performance in promoting cell migration compared with that when dosing IGF-1 or SDF-1 alone, or SDF-1 and IGF-1 together (Fig. S3), which indicated that it could be a combinatory outcome of the various components of SSAD in promoting cellular behaviors.

### 2.3. *In vivo animal studies*

#### 2.3.1. *Hard palate mucosal injury model*

Patients receiving FGG suffer from many complications associated with palatal mucosa defects, such as pain, infection, and discomfort during eating, especially diabetic patients. Although diabetic ulcers have received much attention in recent years, there have been few studies regarding intraoral wound healing in diabetes mellitus patients [22,23]. To the best of our knowledge, this study is the first to load AG for local use to promote palatal wound healing in the presence of hyperglycemia. Due to the moist and unstable environment of the oral cavity, it is impossible for the SSAD hydrogel to stably stay where it is applied over extended periods, and thus a relatively quick release of AG could be a better choice for our intended application *in vivo*, which could improve the bioavailability to the greatest extent. In addition, more liquid was needed for the gelation of the same weight of SSAD powders with the particle size increased, which indicated that SSAD powders with a larger particle size might have a better hemostasis effect (Fig. S4). All these data formed the rationale where 20-mesh SSAD was chosen for treating the palatal mucosal injury model.

In our study, no abnormal physiological symptoms were observed throughout the experimental period. Compared with the other two groups, mice treated with SSAD and SSAD loaded with AG (SSAD + AG) showed less bleeding (Fig. 4a). Furthermore, a classic liver damage-hemostasis model (Fig. S5) indicated that SSAD could effectively adhere to the wound site to seal and stop bleeding (Fig. S6). As revealed in Fig. 4b and Table S2, at 3 days postsurgery, the wound closure rates of the animals in the SSAD + AG group (57.2 ± 9.0%), the AG group (48.9 ± 10.2%), and the SSAD group (49.9 ± 5.6%) were significantly faster than that of mice in the control group (39.8 ± 8.2%), among which the SSAD + AG group healed the fastest. At 7 days postsurgery, the wound closure of the animals in the SSAD + AG group (75.9 ± 6.7%) was still significantly higher than that of those in the control group (53.8 ± 15.4%). At 18 days postsurgery, the wounds in the SSAD + AG group had almost completely healed, with an average wound closure rate of 96.9 ± 3.4%, which was higher than rates in the control group (86.4 ± 9.3%), the SSAD group (92.5 ± 7.1%), and the AG group (91.0 ± 9.2%), and the difference between the SSAD + AG group and the control group was significant ($P < 0.05$). Thus, SSAD + AG greatly accelerated the healing of oral mucosa defects within a relatively short period of time.

Diameter of the full-thickness hard palatal mucosal defect in this study was 3 mm, and we generated the wounds located in the middle of the hard palatals, which was consistent for each rat. Accordingly, we

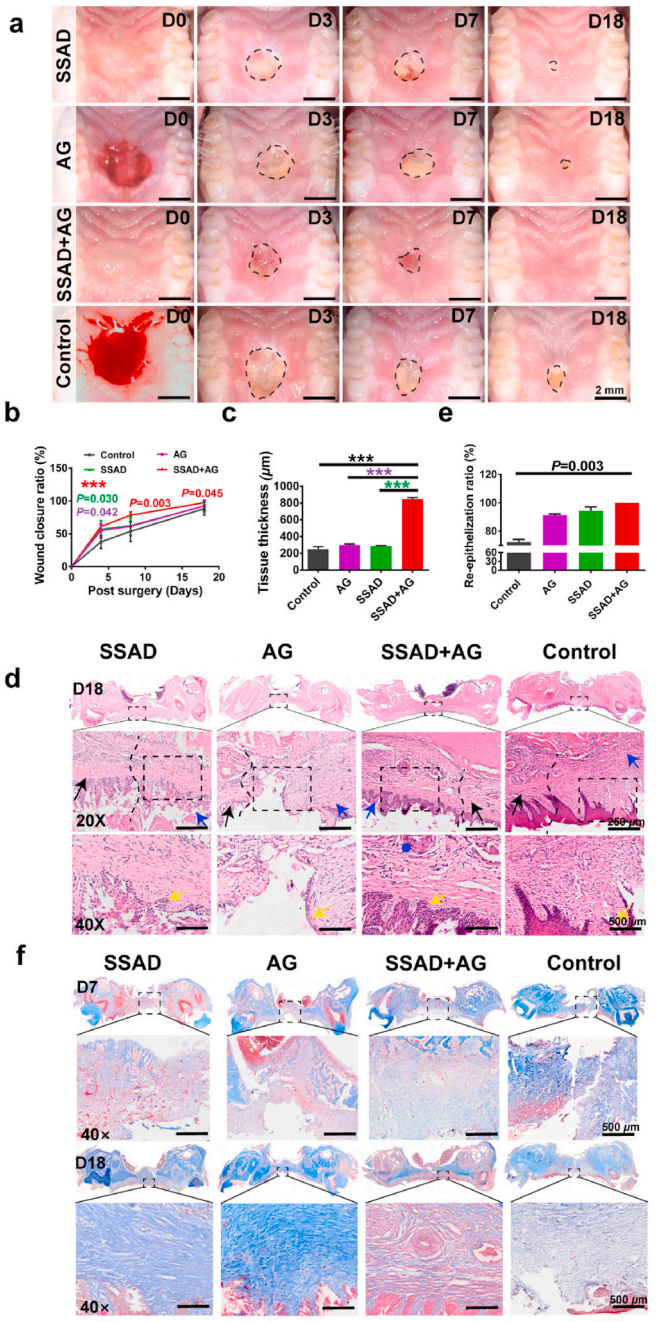


**Fig. 4.** Assessment of the wound healing rates in the palate. (a) Macroscopic observations of wounds. (b) Wound closure rates calculated using Equation (1). (c) Images of HE-staining of the wound sites at 18 days postsurgery. (d) New tissue thicknesses in different groups at 7 days postsurgery. (e) Re-epithelialization rates in different groups at 18 days postsurgery. (f) Images of Masson's trichrome staining of the wound sites at 7 and 18 days. The dashed lines show the boundary between normal and regenerated tissues. Normal tissues (black arrows), regenerated tissues (blue arrows), re-epithelialization (yellow arrows), and gland regeneration (●). (*$P < 0.05$, **$P < 0.01$, ***$P < 0.001$).

could roughly calculate the position of the wound relative to the upper jaw. More importantly, the normal oral tissue consists of epithelium, lamina propria, and submucosa, where small salivary glands (●) are present (Fig. S7). In addition, the regenerated palate mucosa thickness was remarkably higher than that of normal tissues during healing, and the collagen in regenerated tissues was arranged in a relatively disordered manner and showed more cell infiltration (Fig. S8). Therefore, hematoxylin-eosin (HE) staining was conducted to observe mucosal thickness, epithelial integrity, and gland regeneration in the treatment groups, and the black dotted line indicates the boundaries between the normal (black arrows) and the regenerated tissues (blue arrows) (Fig. 4c). Although the regenerated palate mucosa thickness exhibited no statistically significant differences between the four groups at 18 days postsurgery, at 7 days postsurgery, the regenerated palate mucosa thickness in the SSAD + AG group (847.4 ± 17.8 μm) was remarkably higher than that in the SSAD (292.4 ± 11.3 μm), AG (299.6 ± 11.4 μm), and control (248.8 ± 29.8 μm) groups (Fig. S9 and Fig. 4d, $P < 0.001$), which could be attributed to tissue remodeling during wound healing. Specifically, at the early recovery stage, large amounts of extracellular matrix (ECM) are secreted by the migrating and proliferating keratinocytes and fibroblasts at the wound edge, and then, the granulation tissue becomes mature to form a scar, characterized by continued collagen synthesis and collagen catabolism [24].

Epithelial spikes (yellow arrows, Fig. 4c) are a symbol for mucosa healing. According to the standard shown in Fig. S10, we calculated the re-epithelialization rate in each group, and the re-epithelialization rate in the SSAD + AG group (97.2 ± 2.8%) was higher than that in the SSAD (92.1 ± 3.6%), AG (91.5 ± 31.7%), and control (85.5.3 ± 9.6%) groups, and the difference between SSAD + AG and control was significant (Fig. 4e). More interestingly, almost no saliva could be previously regenerated at the full-thickness mucosa defect area [25]. In this study, some salivary glands (●) were observed in the SSAD + AG group but not in the AG, SSAD, or control groups. Appendage regeneration is one of the key indicators of scarless healing [26].

Collagen is the main component of the lamina propria, and the balance between collagen synthesis and degradation plays a vital role in wound regeneration [27]. Masson's trichrome staining was conducted to observe collagen deposition (Fig. 4f). At 7 days postsurgery, which was a relatively early stage of wound healing, the proliferated collagen fibers in the SSAD + AG group were densely packed with a thick bundle morphology. At 18 days postsurgery, the regenerated collagen in the SSAD + AG and SSAD groups was gradually rebuilt to normal levels with a more densely aligned fiber matrix (Figs. 4f and 40 ×), whereas the collagen fibers in the AG and control groups were still in a relatively disordered arrangement (Fig. 4f). The abovementioned data showed that matrix collagen deposition in the SSAD + AG group was gradually rebuilt to normal levels at the later stage of wound healing, indicating that SSAD loaded with AG significantly promoted tissue regeneration under hyperglycemia by accelerating collagen synthesis and maturation. The combined effect was better than that of SSAD or AG alone and far superior to that in the blank control group, and thus, SSAD loaded with AG could be considered an effective approach for promoting diabetic wound healing.

Immunofluorescence staining of relevant biomarkers related to tissue regeneration was also conducted to compare regeneration effects among the four groups. CD31 (red) was used to stain vascular endothelial cells, which demonstrate neovascularization [28]; Col-1 (green) was used to stain collagen, which is a vital marker of ECM deposition [29] (Fig. 5a). α-Smooth muscle actin (α-SMA, red) was used to stain myofibroblasts, which contribute to the contraction of mature vessels [30], and the macrophagocyte marker CD68 (green) was used to assess the inflammation level [31] (Fig. 5b).

At 18 days postsurgery, the expression densities of the $CD31^+$ and Col-1+ cells in each single microscopic view were significantly higher in the SSAD + AG treatment group (38.6 ± 6.5, or 33.0 ± 4.2%) than in the control group (1.2 ± 0.5, or 3.4 ± 1.2%), the SSAD group (16.1 ± 4.0, or 13.1 ± 6.5%), and the AG group (8.9 ± 2.6, or 7.4 ± 2.1%) (Fig. 5c). The expression densities of α-SMA + cells in each microscopic view were significantly higher in the SSAD + AG treatment group (2.1 ± 0.8%) than in the control group (0 ± 0%), the SSAD group (0.7 ± 0.4%), and the AG group (0.3 ± 0.3%) (Fig. 5d). The expression densities of $CD68^+$ cells in each microscopic view in the SSAD + AG treatment group (0.6 ± 0.2%), the SSAD group (1.3 ± 0.3%), and the AG group (1.3 ± 0.3%)

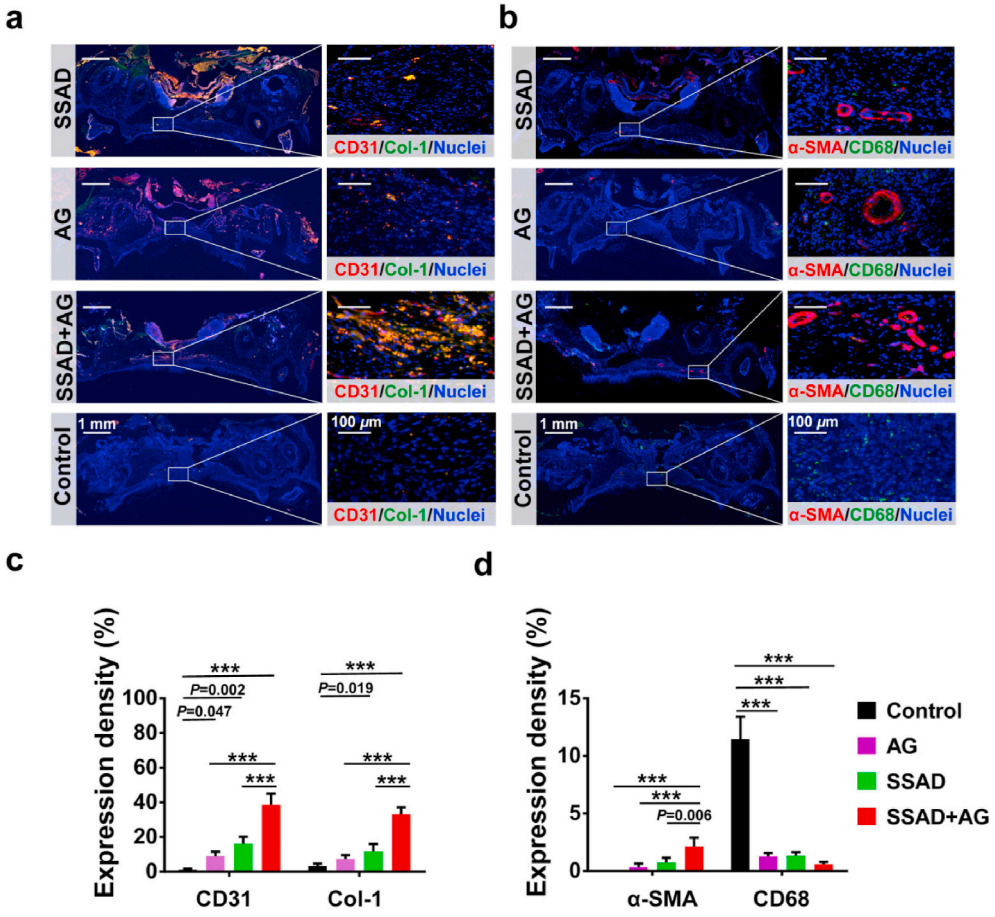


**Fig. 5.** Images of immunofluorescence staining of palatal wounds at 18 days post-surgery. (a) Immunofluorescence staining of vascular endothelial cells (CD31, red) and collagen I (Col-1, green). (b) Immunofluorescence staining of myofibroblasts ($\alpha$-SMA, red) and macrophage (CD68, green). The nuclei were stained with 4′,6-diamidino-2-phenylindole (DAPI, blue), and the double-stained tissues were identified by yellow fluorescence. (c, d) Histograms representing the quantitation of (c) the percentages of $CD31^+$ cells and Col-1 and (d) the percentages of myofibroblasts ($\alpha$-SMA+) and macrophage ($CD68^+$) cells at Day 18.

were significantly lower than in the control group (11.5 ± 2.0%) (Fig. 5d). The separate fluorescence images of Fig. 5a are also provided to evaluate the collagen deposition and neovascularization (Figs. S11 and S12). These findings further demonstrate that SSAD loaded with AG can enhance the performance of SSAD in promoting vascularization, enhancing ECM remodeling, and reducing inflammation [32].

Collectively, by releasing AG in a controllable manner and promoting L929 cell and HUVECs proliferation and migration, SSAD loaded with AG was believed to promote granulation tissue formation and neovascularization by interactions between keratinocytes in the proliferative phase [33].

To further elucidate the underlying mechanisms of SSAD in promoting wound healing, transcriptomics analyses of the regenerated oral mucosa were conducted. The Venn diagram shown in Fig. 6a indicates that 994 differentially expressed genes (DEGs) were coexpressed in the two groups. Heatmaps of the DEGs after SSAD treatment are shown in Fig. 6b. We analyzed the protein–protein interaction (PPI) network corresponding to the coexpressed DEGs, and the color intensity (from blue to red) and size of each node positively represents their degree of linkage with other protein molecules. As shown in Fig. 6c, PPI analysis revealed that the primary relevant signaling molecules were proteins associated with collagens, such as Col1a1, Col3a1, and Col6a1. Kyoto Encyclopedia of Genes and Genomes (KEGG) pathway enrichment analysis of the upregulated DEGs (shown in Fig. 6d) showed that those genes were significantly enriched in collagen protein digestion and absorption, ECM-receptor interactions, and cell adhesion molecules (CAMs), indicating that SSAD can accelerate cell adhesion, collagen deposition, and ECM production. Moreover, although not significant, some genes were also enriched in other signaling pathways, such as those regulating the pluripotency of stem cells, reminding us that SSAD may also promote wound healing by recruiting stem cells. Functional enrichment analysis was carried out based on the KEGG database, and the top 20 gene ontology (GO) terms are shown in Fig. 6e, among which the significantly enriched biological processes were ECM formation related to cell-matrix adhesion, cell adhesion and migration, ECM organization, collagen fibril organization, multicellular organism development, and positive regulation of cell-substrate adhesion. All of the above transcriptome results were verified by immunofluorescence staining with the corresponding antibodies. The results in Fig. 5 show that after SSAD treatment, there were high positive staining rates for Col-1, CD31, and $\alpha$-SMA in the SSAD-related groups, consistent with the transcriptome data. This outcome indicates that pathways and biological processes associated with wound healing were activated by SSAD treatment, such as ECM-receptor interactions, cell-matrix adhesion, and ECM organization.

Wound healing can generally be divided into four stages: hemostasis, inflammation, cell proliferation, and tissue remodeling [33]. Activation and efficient recruitment of stem cells toward the wound area are critical contributors to wound re-epithelialization [34,35]. Owing to their capacity to differentiate into a variety of functional cells [36], keratinocyte stem cells (KSCs) homing to wound sites play a vital role in wound healing and can maintain and repair epithelial tissue and retain the proliferative potential of the tissue [37,38]. Our bioassay results showed that SSAD contained a large number of growth factors, such as VEGF, IGF-1, and SDF-1 (Table S1). Most growth factors are thought to promote cell proliferation and migration, thereby promoting wound healing. In particular, SDF-1 recruits stem cells to wound sites [39], where they differentiate into endothelial cells and fibroblasts, turning into myofibroblasts via cell activation/proliferation or mesenchymal transition, which play key roles in soft tissue regeneration [40]. Moreover, the expression of IGF-1 also plays an important role in mediating wound healing [41]. In this study, to further verify whether SSAD can recruit

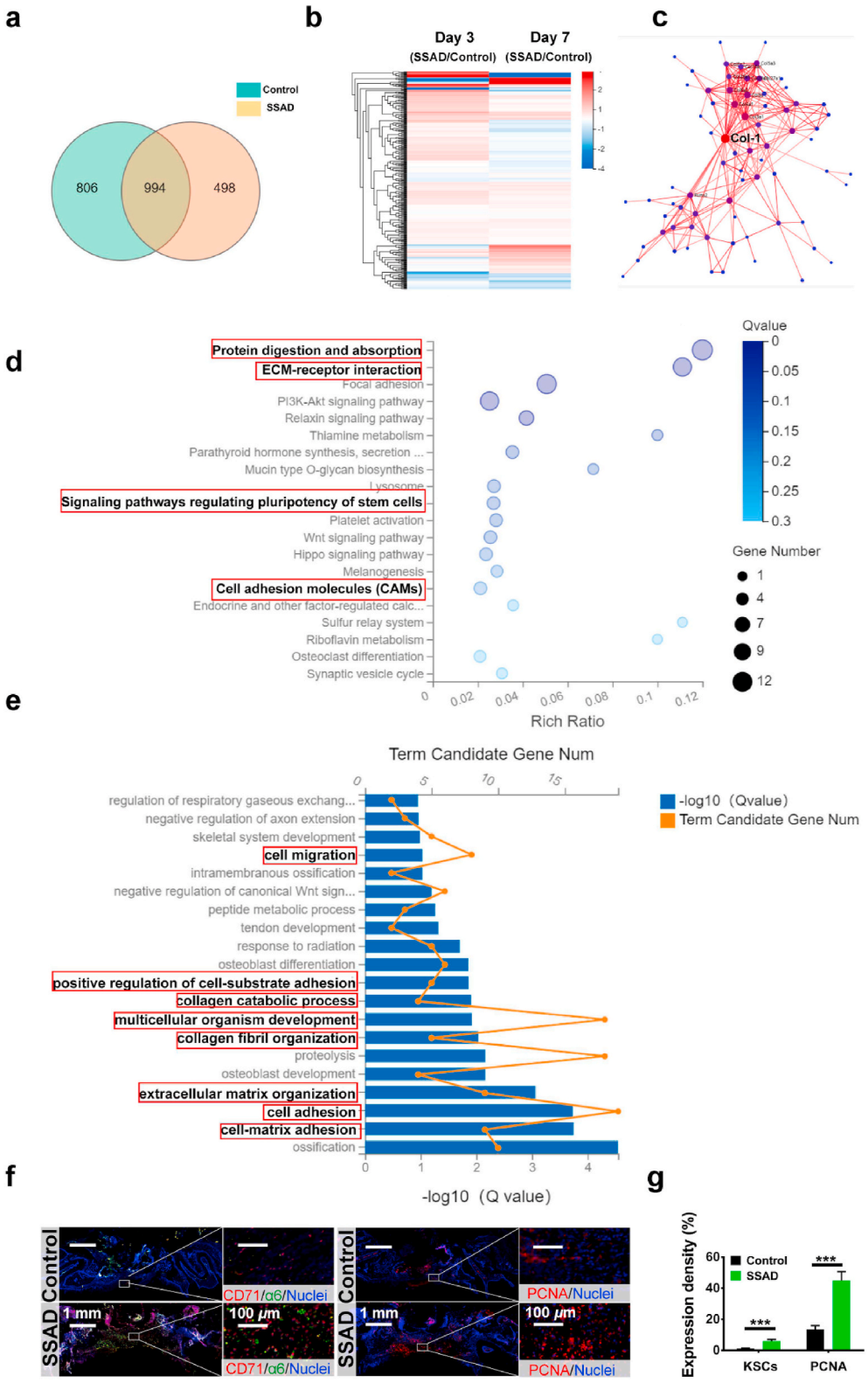


**Fig. 6.** Therapeutic mechanisms of SSAD in wound healing. (a) Venn diagram of the transcriptomic profiles between the SSAD and control groups. (b) Heat maps of significantly changed genes after SSAD treatment ($|\log| \geq 2$, $P < 0.05$). (c) The KEGG pathway and (d) the 20 most significantly enriched biological processes. (e) Enrichment analyses of the identified differentially expressed genes in the protein–protein interaction network of the differentially expressed genes based on the KEGG database. (f) Immunofluorescence staining of KSCs ($\alpha$6+, green/CD71-, red) and proliferative cells (PCNA+, red) at Day 7. (g) Histograms representing the quantitation of the percentages of KSCs ($\alpha$6+/CD71-) and PCNA + cells.

endogenous stem cells and activate cell adhesion and migration pathways, as suggested by the above transcriptome analyses, we assessed stem cell recruitment and cell proliferation in the regenerated tissues via immunofluorescence.

Immunofluorescence staining of KSCs ($\alpha$6+/CD71-) [37,42,43] and proliferating cell nuclear antigen (PCNA) staining [44] were conducted and compared between the SSAD-treated group and the blank control group. The results (Fig. 6f and g) showed that significantly more KSCs were recruited to the wound sites in the SSAD-treated group than in the control group ($P < 0.001$) at 7 days postsurgery. The number of PCNA + keratinocytes in the SSAD-treated group was also significantly greater in the SSAD-treated group than in the control group at the same time point ($P < 0.001$).

Based on these results, we concluded that SSAD could promote KSC

recruitment to wound sites and maintain a larger pool of regenerative epithelial keratinocytes that function in accelerating wound healing. Moreover, SSAD could promote cell adhesion and ECM and collagen deposition, making it a promising dressing for soft tissue regeneration.

### 2.3.2. *Tumor-bearing wound healing model*

In our study, encouraged by the outstanding *in vitro* drug-loading and controlled-release performance, we further proposed the idea of synergistically combining local chemotherapy with tissue regeneration in treating skin tumors. As for the tumor-bearing wound healing model, considering the strong irritation associated with topical application of DOX, under the conditions that the total dosage of DOX were same, a relatively lower release rate of DOX might benefit the melanoma-bearing wound healing *in vivo*, and thus we eventually chose the 200-mesh SSAD hydrogel, which could release drugs more sustainably. The incidence of malignant melanoma is on the rise in many areas, and melanoma can occur in the skin or mucosa [45,46]. Cutaneous malignant melanoma is most common in Caucasians, while mucosal malignant melanoma is most common in yellow people (e.g., Japanese) [47]. Malignant melanoma in the oral cavity mostly occurs in the upper gingiva and hard palate [47]. Therefore, melanoma was chosen as the tumor model.

B16F10 tumor-bearing mice were randomized into 4 groups: control, SSAD, DOX, and SSAD + DOX. Photographs of tumor-bearing wound healing at the indicated time points are shown in Fig. 7a. Photographs of the excised tumors 18 days after various treatments (Fig. 7b) further visually illustrate the therapeutic effect in each group.

The tumors resected from the mice in each group were also weighed (Fig. 7c) and sized (Fig. 7d). The average tumor size in the control group increased rapidly and exceeded 2,580 $mm^3$ and 1.9 g at 18 days, with the highest tumor recurrence rate (up to 67%) (Fig. 7e). Interestingly, the tumor volume in the SSAD hydrogel group increased more slowly, and the average tumor size (691 $mm^3$, 0.3 g) was smaller than that in the control group, with a 44% tumor recurrence rate, verifying that SSAD

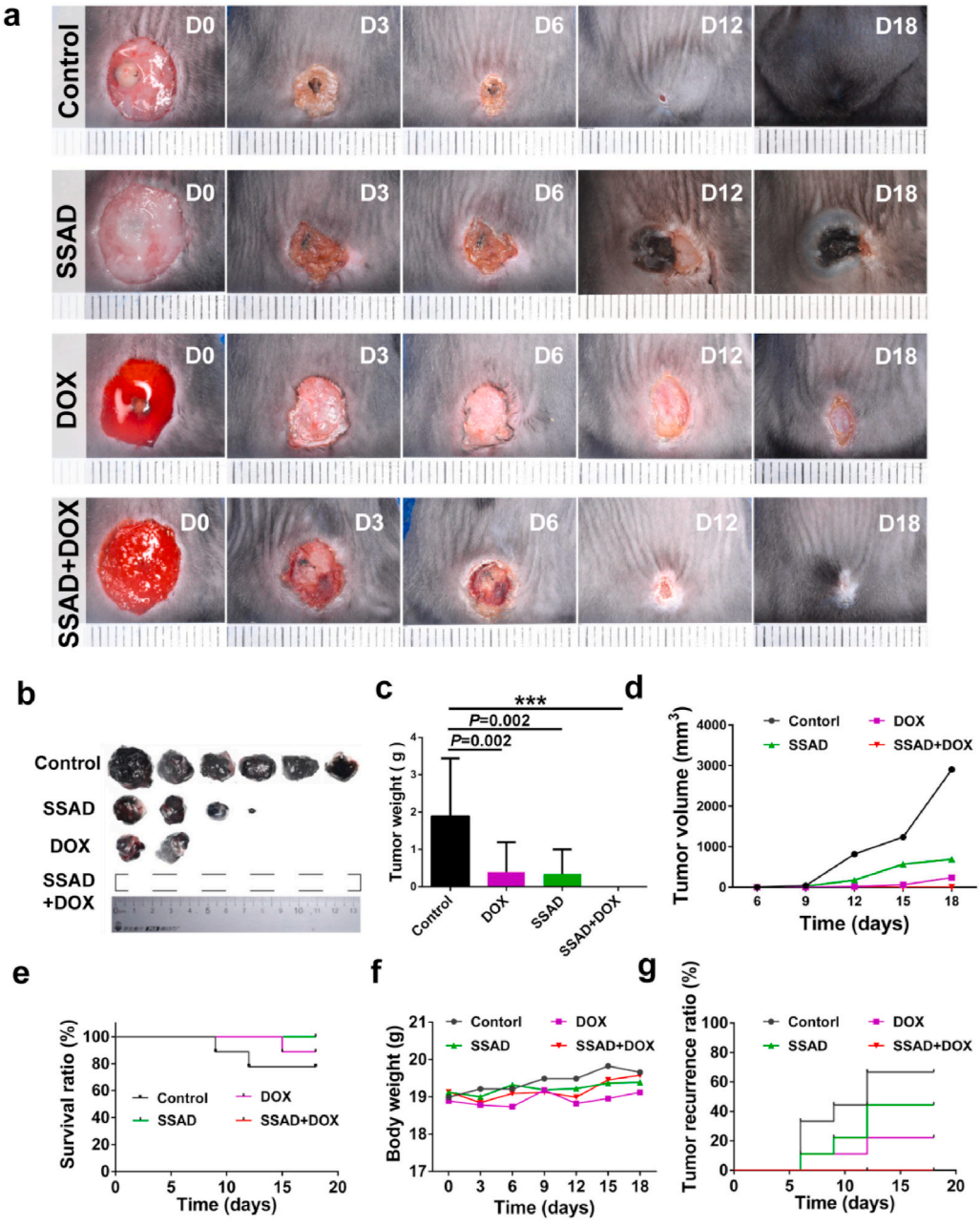


**Fig. 7.** *In vivo* anticancer efficiency of the DOX-loaded SSAD hydrogel. (a) Macroscopic observation of tumor-bearing wounds under four different treatments. (b) Photographs and (c) weights of the resected tumors at 18 days after various treatments. (d) Growth curves of tumors in the different groups after the various treatments. (e) Tumor recurrence curves, (f) body weight curves, and (g) survival curves of the mice in the different treatment groups (n = 9, $^*P < 0.05$, $^{**}P < 0.01$, $^{***}P < 0.001$).

itself already exhibits antitumor activity to some extent. A slightly more obvious inhibition of the tumors (239 $mm^3$, 0.4 g) was observed in the DOX group, with a 22% recurrence rate, compared with the control group. However, strikingly no mice in the SSAD + DOX group exhibited tumor recurrence during the period evaluated (Fig. 7e). Meanwhile, no obvious abnormalities in body weight were found in any of the four groups (Fig. 7f). During the entire treatment duration, the tumor-bearing mice in the control, DOX, and SSAD groups survived at rates of 78%, 89%, and 100%, respectively, whereas mice in the SSAD + DOX treatment group not only survived at a rate of 100% but also remained tumor-free (Fig. 7g).

These encouraging results indicate that the tumor cells could be effectively eliminated in the SSAD + DOX group by the DOX released from the SSAD hydrogel during the early stage and that the ability of SSAD to cure full-thickness skin defects was not significantly affected by the relatively short period of DOX treatment. Although normal skin cells near DOX-loaded SSAD might also be ablated by DOX release, SSAD could induce many types of cells from relatively healthy tissues to migrate to the wound site, where they can participate in the subsequent wound healing process. This synergy played an important role in the subsequent tissue healing process. More importantly, SSAD contains a large number of growth factors that recruit stem cells and activate wound healing-related signaling pathways and biological processes during wound healing, consequently promoting neovascularization, ECM production, and collagen deposition. Meanwhile, the mild tumor-suppressive effect of SSAD itself might be attributed to immune regulation of the recruited stem cells [48,49]. In addition, the SSAD hydrogel made of 200-mesh fine particles could limit the exchange of nutrients and metabolites. Although the limitation could be very weak and had no obvious effects on normal tissues, solid tumors that require more nutrients and oxygen and produce more waste products during fast growth could be more susceptible.

Finally, HE, terminal-deoxynucleotidyl transferase-mediated nick end labeling (TUNEL), and Ki67 staining of the tumor tissues at 18 days were performed (Fig. 8a). Images of HE staining revealed that the SSAD + DOX group induced the most tumor cell destruction. As demonstrated by TUNEL staining, the SSAD + DOX group had the highest expression of apoptotic fluorescence compared with the other three groups. Moreover, Ki67+ tumor cell expression in the SSAD + DOX group was almost invisible, suggesting a pronounced reduction in tumor cell proliferation with the SSAD wound dressing loaded with DOX. Quantitative analyses of the apoptotic cells and Ki67+ tumor cells are shown in Fig. 8b and c. Overall, it was obvious that SSAD + DOX showed the best inhibition of melanoma compared with the other groups *in vivo*. Moreover, there were no clear histopathological changes in the major organs after the different treatments in this study (Fig. 8d), which suggests that SSAD could be used as a safe vehicle for localized drug delivery.

## 3. Conclusion

In summary, the SSAD hydrogels were proven to be an effective local drug sustained-release system for AG and DOX based on the particle sizes of the SSAD powders forming the corresponding hydrogels. Moreover, the effects of SSAD, shown to promote cell migration and proliferation, accelerate ECM deposition, and recruit endogenous stem cells to wound sites, were further studied. Our unique SSAD wound dressing system shows considerable potential as a local drug delivery system for sustained drug release and wound healing promotion. However, because of the limited laboratory conditions, it was not possible to track the drug release by SSAD in real time *in vivo*. In addition, although our study revealed that there were more collagen deposition and stem cell recruitment at the wound sites after SSAD treatment, the types of cells that were most activated or inhibited in the process of wound healing still remain unknown. In the follow-up studies, we may need to further investigate into single-cell transcriptomes to explore the specific pro-healing mechanisms of SSAD in tissue regeneration.

## 4. Materials and methods

### 4.1. SSAD preparation and characterization

#### 4.1.1. SSAD preparation, SEM, and FT-IR measurement

The dorsal mucus was collected from the Chinese giant salamander, as we described previously [17]. In brief, the Chinese giant salamander began to secrete mucus under mechanical stimulation (gently scratching its skin). After the mucus was collected into a clean tube, it was washed with sterilized PBS, shaken, and centrifuge. Next, the mucus was freeze-dried for 24 h, ground into powder by a freezing ball milling machine at 0 °C for different times, and finally divided into different particle sizes using the corresponding mesh sizes (20, 60, and 200 meshes).

The SSAD powders and drug (AG or DOX)-loaded hydrogels with different pore sizes were examined *via* SEM and FT-IR. SSAD powders and freeze-dried SSAD hydrogels with different sizes (20, 60, and 200 mesh) were installed on the holders. After gold sputter coating, all samples were imaged via SEM (SU8010, ZEISS MERLIN Compact, Japan) at 10 kV and 5 kV. The FT-IR spectra (4000-400 $cm^{-1}$) of AG, DOX, and the drug-loaded SSAD hydrogels were recorded using an FT-IR spectrometer (Nicolet 670, USA) in transmission mode, and the spectral data were recorded as absorbance units.

#### 4.1.2. SSAD hydrogel degradation experiments

The degradation ratios of the SSAD hydrogels derived from different particle sizes (20, 60, and 200 mesh) were evaluated in PBS and human saliva. In brief, 100 mg of SSAD was gelled with PBS. Afterward, the hydrogels were soaked in PBS or human saliva (5 mL). For the SSAD hydrogel degradation experiments, SSAD hydrogel was collected at a predetermined time point and freeze-dried for 24 h. The degradation ratio was calculated according to Equation (1):

$$\text{Degradation } ratio = \frac{W_t - W_b}{W_b} \times 100\% \quad (1)$$

where $W_t$ represents the weight of the SSAD hydrogel lyophilized after swelling in PBS or human saliva at different time intervals, and $W_b$ represents the weight of the SSAD powders at baseline.

#### 4.1.3. Controlled release of drugs in vitro

The release kinetics of the SSAD hydrogels with different particle sizes (20, 60, and 200 meshes) were evaluated using AG or DOX. In brief, 50 mg of AG or 10 mg of DOX was mixed with 500 mg of SSAD or 1,000 mg of SSAD (20, 60, or 200 meshes) to form an SSAD-loaded hydrogel in PBS. Afterward, the drug-loaded hydrogels were soaked in PBS (5 mL, pH 7.4). At the predetermined time points, the samples were collected and detected at wavelengths of 230 nm or 480 nm to determine the concentrations of AG or DOX. Meanwhile, the same volume of PBS was added back to each test tube to maintain a constant volume.

### 4.2. Cell proliferation and migration assays

#### 4.2.1. CCK-8 assay

A total of 5,000 cells in 200 μL ofmedium were seeded in each well of 96-well plates. After incubation for 24 h in an incubator (37 °C, 5% $CO_2$), the culture medium was replaced with 200 μL of SSAD-containing hydrogel for 12 and 24 h. At the indicated time points, 100 μL of fresh DMEM and 10 μL of CCK8 solution were added to each well for a 2-h incubation at 37 °C, and the absorbance at 450 nm was measured using a microplate reader (EnSpire, PerkinElmer, Singapore).

#### 4.2.2. Scratch wound-healing assay

For the scratch assay, $6 \times 10^5$ cells were seeded in each well of a 6-well plate, and after they had reached confluence, they were wounded with a 200-μL pipette tip followed by washing with PBS three times and

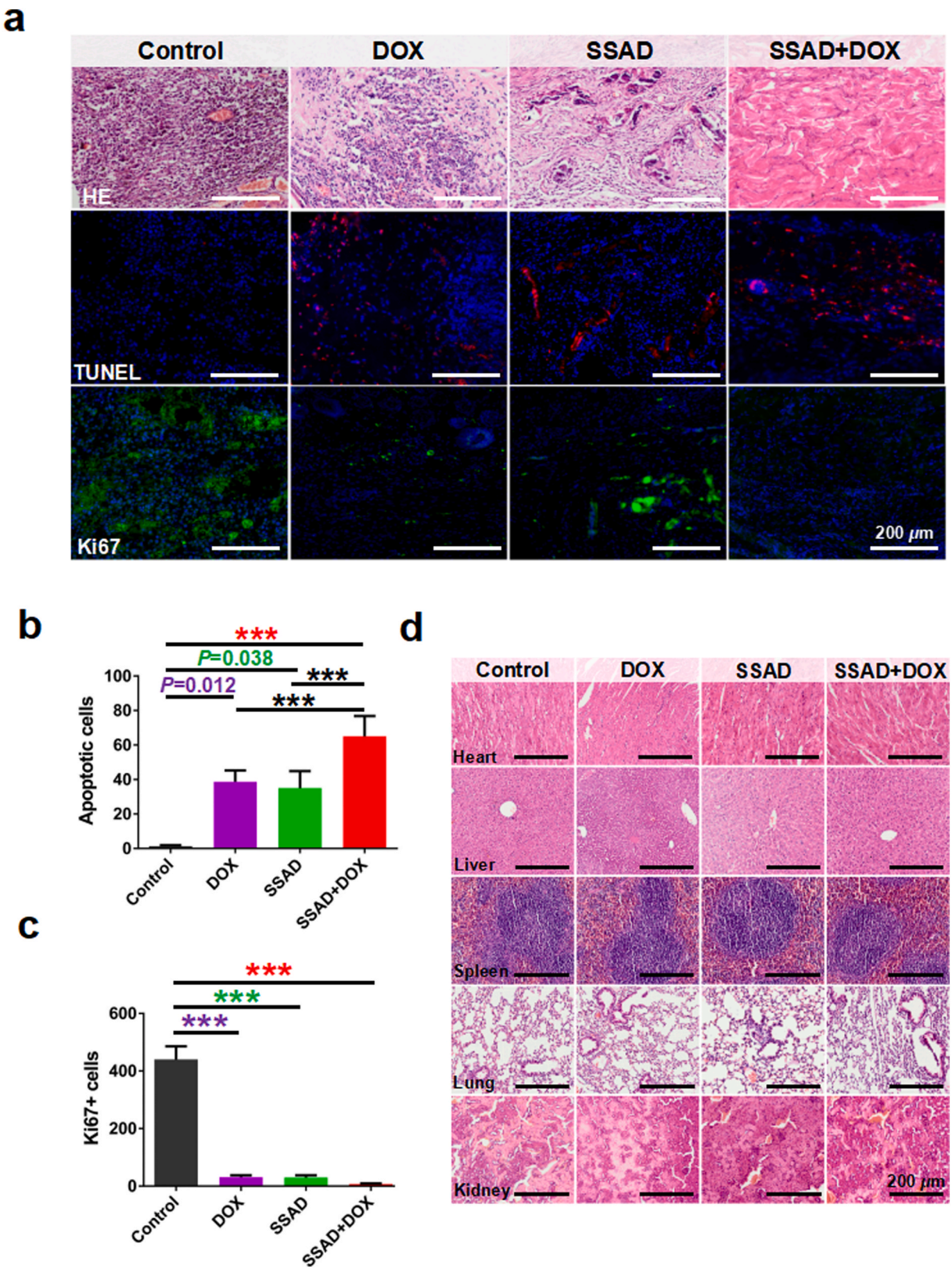


**Fig. 8.** *In vivo* microscopic anticancer efficacy. (a) Images of HE staining, TUNEL staining, and Ki67 staining (red: apoptotic cells; green: Ki67+ cells; blue: nuclei) of the tumor tissues in the different groups. Quantification of (b) the expression of Ki67 and (c) TUNEL assay results (cell numbers in each visual field). (d) Representative histological images of the main organs with HE staining (*$P < 0.05$, **$P < 0.01$, ***$P < 0.001$).

then incubation with DMEM containing SSAD for 24 h. The cells were photographed under a microscope at 0 and 24 h.

#### 4.2.3. Transwell migration assay

Based on the scratch wound healing results, we then conducted a Transwell migration assay. Briefly, 100 μL of DMEM containing $2 \times 10^5$ cells (L929 or HUVECs) was seeded in the top chamber of the insert, and the bottom chamber was loaded with 800 μL of DMEM supplemented with SSAD. After incubation for 24 h, the inserts were removed and washed, and the cells that had migrated to the lower side of the membrane were stained with 0.1% crystal violet and counted under a microscope as previously described [50].

### 4.3. Animal studies

#### 4.3.1. Hard palate mucosal wound healing model with hyperglycemia

Animals were purchased from the Experimental Animals Center of Chongqing Medical University and housed under specific pathogen-free (SPF) conditions at the animal experimental center of the Stomatological Hospital of Chongqing Medical University. The animal experiments were approved by the Stomatological Hospital of Chongqing Medical University Animal Use and Care Committee (CQHS-REC-2020–021).

Forty (8–12 weeks) male Sprague–Dawley (SD) rats weighing an average of 200–220 g were used in this study, and type 2 diabetes mellitus was induced by intraperitoneal injection of streptozotocin (STZ, 60 mg/kg). At 1 week after STZ injection, only rats with blood glucose levels higher than ≥250 mg/dL were included in the subsequent study [23]. Hard palate mucosal injury was induced as described by First and colleagues [51]. Briefly, all animals were anesthetized intraperitoneally with 1% pentobarbital sodium (30 mg/kg). Then, a blepharostat was used to open the mouth, and the palatal mucosa was disinfected with iodine and 75% ethanol. Next, a full-thickness hard palatal mucosal defect was created in the rat palate (located in the middle) with a disposable biopsy punch (diameter = 3 mm). All animals were randomly divided into the following four groups and treated according to their group (n = 10):

- Control group: blank control where no treatments were used
- AG group: AG (0.4 mg per site) [10,52,53].
- SSAD group: SSAD hydrogel (5 mg of SSAD powder per site)
- SSAD + AG group: SSAD hydrogel loaded with AG (5 mg of SSAD powder + 0.4 mg AG per site)

These treatments were repeated daily. Moreover, local AG used in this study (0.4 mg per site) should have a negligible systemic drug effect, which was only 2% of some reported systemic administrating dosages of AG (100 mg/kg) for promoting palatal wound-healing [8].

Photographs of the wound were taken with a digital camera (Nikon, JY67ON, Japan) at the indicated time points, and the digital photographs were transferred to a computer for analyses of palatal incision closure using ImageJ software (National Institutes of Health, NIH, USA). The wound closure rate was calculated according to Equation (2):

$$\text{Wound closure percentage} = \frac{S_{initial} - S_{current}}{S_{current}} \times 100\% \quad (2)$$

where $S_{initial}$ is the initial wound size and $S_{current}$ is the current wound size. Each wound was measured 3 times, and the average wound size was recorded. At 7 and 18 days after surgery, 5 rats in each group were euthanized to harvest the hard palate for histological analysis.

The samples were fixed in 4% paraformaldehyde for 24 h and decalcified in 10% ethylenediaminetetraacetic acid (EDTA, pH 8.0) for 2–3 months. Afterward, they were dehydrated with graduated concentrations of ethanol (60–100%). Subsequently, the specimens were embedded in paraffin and cut into 5-μm sections. For each sample, more than ten slides were prepared, and the wound area of each specimen was sampled perpendicular to the midline of the palate. Then, we chose the sections that exhibited relatively wider wounds for histological analyses and stained them with HE (Solarbio, China) and Masson's trichrome (Solarbio).

The re-epithelialization rate was measured at 18 days postsurgery and was calculated according to Equation (3):

$$\text{Re} - \text{epithelialization rate} = \frac{D_b - D_n}{D_b} \times 100\% \quad (3)$$

where $D_b$ represents the distance of the mucosa defect at baseline (3 mm) and $D_n$ represents the distance without epithelization (Fig. S10) at 18 days postsurgery.

Moreover, immunofluorescence staining was performed. After the sections were blocked with 3% bovine serum albumin (BSA, A8020, Solarbio), they were immunostained with primary antibodies (Abcam, USA) at 4 °C overnight. Then, after incubation with the corresponding secondary antibodies (Abcam) for 1 h at room temperature, the nuclei were counterstained with DAPI (Goodbio Technology Co., Ltd., China). All images were acquired with an inverted fluorescence microscope (Nikon, Nikon Eclipse Ti-SR, Japan).

To further elucidate the mechanism of SSAD in promoting wound healing, we assessed cell proliferation in the repaired tissues using PCNA staining and conducted transcriptomics analyses. SD rats with the established palatal mucosal defect model (diameter = 3 mm) were randomly grouped into SSAD (receiving SSAD dressing, n = 16) and control (no treatment, n = 16) groups. On Day 3 and Day 7, half of the rats (n = 8) in each group were sacrificed, and the palatal mucosa was collected for transcriptome analysis. RNA extraction, purification, reverse transcription, library construction, and sequencing were all performed at Shenzhen BGI Co. Ltd. (Shenzhen, China).

After completing the sequencing, we conducted bioinformatic analyses based on the database we obtained, and the expression level of the genes was calculated using RSEM (v1.2.12). Differential expression analysis was performed using PossionDis with a false discovery rate (FDR) ≤ 0.001 and |Log2Ratio| ≥ 1. Venn diagrams were used to detect the coexpressed genes in the two groups. To gain insight into the change in phenotype, GO and KEGG enrichment analyses (http://www.geneontology.org/and https://www.kegg.jp/, respectively) of the coexpressed genes in both groups were performed using Phyper based on hypergeometric tests (https://en.wikipedia.org/wiki/hypergeometric_distribution). The significance levels of the terms and pathways were corrected with a Q value ≤ 0.05 via Bonferroni correction. In addition, PPI network analyses of the coexpressed genes were performed using the Search Tool for the Retrieval of Interacting Genes/Proteins algorithm.

#### 4.3.2. Antitumor efficacy and wound-healing model

Thirty-six female C57BL/6 mice (8–10 weeks) were used in this study [54]. The tumors were created by injection of 1 × 106 B16F10 cells [54] into the back of each C57BL/6 mouse after fur removal from the injection site. When the tumor reached approximately 50 $mm^3$, the tumor-bearing C57BL6 mice were randomly grouped as follows (n = 9):

- Control group: blank control where no treatments were used
- DOX group: DOX (4 mg/kg per site) [54].
- SSAD group: SSAD hydrogel (8 mg of SSAD powder per site)
- SSAD + DOX group: SSAD hydrogel loaded with DOX (8 mg of SSAD powder + 4 mg/kg DOX per site)

Then, a circular full-thickness skin defect of 10 mm was created at each tumor site, and the corresponding material for each group was used to cover this wound created by tumor removal. Considering that tumor-bearing wounds in this study would experience scabbing under a relatively dry environment, they were only treated at day 0 with a reasonable dosage of drugs to avoid stimulating the wounds repeatedly. After treatment, the mouse body weights, tumor sizes and survival rates were

recorded every two days. The tumor sizes were calculated according to Equation (4):

$$\text{Tumor volume} = \frac{L \times W \times W}{2} \quad (4)$$

where L represents the tumor length and W represents the tumor width.

At 18 days after treatment, the mice were sacrificed, and the tumors were collected, weighed and photographed. After a series of routine treatments (tissue fixation, dehydration, embedding, slicing), tissue sections from the four groups were selected and stained with HE for histological analyses. Ki67 immunohistochemistry was used to evaluate the proliferation of tumor cells. We also performed a TUNEL assay to detect any apoptotic tumor cells.

### 4.4. Statistical analyses

All data are shown as the means ± standard errors of the means. Statistical analyses were carried out with GraphPad Prism software (GraphPad Software, USA). Statistical significance was evaluated using one-way analysis of variance (ANOVA) or an unpaired *t*-test. Significance was established for $P$ values $< 0.05$.

## CRediT authorship contribution statement

**Xiang Liu:** Validation, Investigation, Data curation, Software, Writing – original draft. **Xiang Mao:** Writing – review & editing, Visualization, Supervision. **Guo Ye:** Visualization, Supervision. **Menghong Wang:** Visualization, Supervision. **Ke Xue:** Visualization, Supervision. **Yan Zhang:** Methodology, Supervision. **Hongmei Zhang:** Visualization, Supervision. **Xiaoqiao Ning:** Investigation. **Man Zhao:** Visualization, Supervision. **Jinlin Song:** Conceptualization, Supervision. **Yu Shrike Zhang:** Visualization, Supervision, Writing – review & editing. **Ximu Zhang:** Conceptualization, Methodology, Validation, Supervision, Writing – review & editing, Funding acquisition.

## Declaration of competing interest

The authors declare no competing interests.

## Acknowledgments

This work was supported by the National Natural Science Foundation of China (32070826, 81801929), the Chinese Postdoctoral Science Foundation (2019M650239, 2020T130762), the Chongqing Research Program of Basic Research and Frontier Technology (cstc2018jcyjAX0807), the Innovative Talents Project of Chongqing Postdoctoral Foundation (YRSB(2019)298), the Chongqing Medical Joint Research Project of Chongqing Science and Technology Committee & Health Agency (2020GDRC017), Chongqing Graduate Tutor Team Project (dstd201903) and the Medical Research Project of Chongqing Health and Family Planning Commission (2017ZDXM016). Y.S.Z was not supported by any of these funds; instead, the Brigham Research Institute is acknowledged.

## Appendix A. Supplementary data

Supplementary data to this article can be found online at https://doi.org/10.1016/j.bioactmat.2021.11.030.

## References

[1] B. Ongnok, N. Chattipakorn, S.C. Chattipakorn, Doxorubicin and cisplatin induced cognitive impairment: the possible mechanisms and interventions, Exp. Neurol. 324 (2020) 113118.
[2] N. Oliva, J. Conde, K. Wang, N. Artzi, Designing hydrogels for on-demand therapy, Acc. Chem. Res. 50 (4) (2017) 669–679.
[3] J. Katz, I. Bhattacharyya, F. Farkhondeh-Kish, F.M. Perez, R.M. Caudle, M.W. Heft, Expression of the receptor of advanced glycation end products in gingival tissues of type 2 diabetes patients with chronic periodontal disease: a study utilizing immunohistochemistry and RT-PCR, J. Clin. Periodontol. 32 (1) (2005) 40–44.
[4] Y. Li, Y. Chang, N. Ye, D. Dai, Y. Chen, N. Zhang, G. Sun, Y. Sun, Advanced glycation end products inhibit the proliferation of human umbilical vein endothelial cells by inhibiting cathepsin D, Int. J. Mol. Sci. 18 (2) (2017).
[5] U.A. Okonkwo, L.A. DiPietro, Diabetes and wound angiogenesis, Int. J. Mol. Sci. 18 (7) (2017).
[6] Y. Bao, H. Chen, Z. Cai, J. Zheng, J. Zou, Y. Shi, L. Jiang, Advanced glycation end products inhibit neural stem cell differentiation via upregualtion of HDAC3 expression, Brain Res. Bull. 159 (2020) 1–8.
[7] Y. Li, L. Wang, M. Zhang, K. Huang, Z. Yao, P. Rao, X. Cai, J. Xiao, Advanced glycation end products inhibit the osteogenic differentiation potential of adipose-derived stem cells by modulating Wnt/β-catenin signalling pathway via DNA methylation, Cell Prolif 53 (6) (2020), e12834.
[8] P.C. Chang, S.C. Tsai, Y.H. Jheng, Y.F. Lin, C.C. Chen, Soft-tissue wound healing by anti-advanced glycation end-products agents, J. Dent. Res. 93 (4) (2014) 388–393.
[9] P.J. Thornalley, Use of aminoguanidine (Pimagedine) to prevent the formation of advanced glycation endproducts, Arch. Biochem. Biophys. 419 (1) (2003) 31–40.
[10] F. Benencia, M.C. Courrèges, G. Gamba, H. Cavalieri, E.J. Massouh, Effect of aminoguanidine, a nitric oxide synthase inhibitor, on ocular infection with herpes simplex virus in Balb/c mice, Invest. Ophthalmol. Vis. Sci. 42 (6) (2001) 1277–1284.
[11] B.O. Nilsson, Biological effects of aminoguanidine: an update, Inflamm. Res. 48 (10) (1999) 509–515.
[12] Y. Sezgin, M. Bilgin Çetin, Ş. Bulut, N. Alptekin, P. Börçek, Evaluating the effects of a topical preparation with dexpanthenol, silbiol, undecylenic acid, and lidocaine on palatal mucosa wound healing in a rat model, Balkan Med. J. 36 (2) (2019) 88–95.
[13] T. Wu, D. Zhang, Q. Qiao, X. Qin, C. Yang, M. Kong, H. Deng, Z. Zhang, Biomimetic nanovesicles for enhanced antitumor activity of combinational photothermal and chemotherapy, Mol. Pharm. 15 (3) (2018) 1341–1352.
[14] J. Li, M. Xin, Y. Huo, A. Cai, M. Yan, C. Wang, G. Wei, Synthesis of β-cyclodextrin-PEG-G molecules to delay tumor growth and application of β-cyclodextrin-PEG-G aggregates as drug carrier, Carbohydr. Polym. 229 (2020) 115478.
[15] J. Chen, J. Ding, W. Xu, T. Sun, H. Xiao, X. Zhuang, X. Chen, Receptor and microenvironment dual-recognizable nanogel for targeted chemotherapy of highly metastatic malignancy, Nano Lett. 17 (7) (2017) 4526–4533.
[16] S.-S. Feng, S. Chien, Chemotherapeutic engineering: application and further development of chemical engineering principles for chemotherapy of cancer and other diseases, Chem. Eng. Sci. 58 (18) (2003) 4087–4114.
[17] J. Deng, Y. Tang, Q. Zhang, et al., A bioinspired medical adhesive derived from skin secretion of Andrias davidianus for wound healing, Adv. Funct. Mater. 29 (31) (2019).
[19] D.T. Graves, N. Nooh, T. Gillen, M. Davey, S. Patel, D. Cottrell, S. Amar, IL-1 plays a critical role in oral, but not dermal, wound healing, J. Immunol. 167 (9) (2001) 5316–5320.
[20] Z. Zhang, Q. Dai, Y. Zhang, H. Zhuang, E. Wang, Q. Xu, L. Ma, C. Wu, Z. Huan, F. Guo, J. Chang, Design of a multifunctional biomaterial inspired by ancient Chinese medicine for hair regeneration in burned skin, ACS Appl. Mater. Interfaces 12 (11) (2020) 12489–12499.
[21] A. Shabbir, A. Cox, L. Rodriguez-Menocal, M. Salgado, E. Van Badiavas, Mesenchymal stem cell exosomes induce proliferation and migration of normal and chronic wound fibroblasts, and enhance angiogenesis in vitro, Stem Cell. Dev. 24 (14) (2015) 1635–1647.
[22] B.K. Fesseha, C.J. Abularrage, K.F. Hines, R. Sherman, P. Frost, S. Langan, J. Canner, K.C. Likes, S.M. Hosseini, G. Jack, C.W. Hicks, S. Yalamanchi, N. Mathioudakis, Association of hemoglobin A(1c) and wound healing in diabetic foot ulcers, Diabetes Care 41 (7) (2018) 1478–1485.
[23] M. Long, M. Rojo de la Vega, Q. Wen, M. Bharara, T. Jiang, R. Zhang, S. Zhou, P. K. Wong, G.T. Wondrak, H. Zheng, D.D. Zhang, An essential role of NRF2 in diabetic wound healing, Diabetes 65 (3) (2016) 780–793.
[24] S. Werner, R. Grose, Regulation of wound healing by growth factors and cytokines, Physiol. Rev. 83 (3) (2003) 835–870.
[25] S.A. Ballestas, T.C. Turner, A. Kamalakar, Y.C. Stephenson, N.J. Willett, S. L. Goudy, E.A. Botchwey, Improving hard palate wound healing using immune modulatory autotherapies, Acta Biomater. 91 (2019) 209–219.
[26] M. Takeo, W. Lee, M. Ito, Wound healing and skin regeneration, Cold Spring Harb. Perspect. Med. 5 (1) (2015) a023267.
[27] X. Zhao, H. Wu, B. Guo, R. Dong, Y. Qiu, P.X. Ma, Antibacterial anti-oxidant electroactive injectable hydrogel as self-healing wound dressing with hemostasis and adhesiveness for cutaneous wound healing, Biomaterials 122 (2017) 34–47.
[28] T. Lucas, F. Schäfer, P. Müller, S.A. Eming, A. Heckel, S. Dimmeler, Light-inducible antimiR-92a as a therapeutic strategy to promote skin repair in healing-impaired diabetic mice, Nat. Commun. 8 (2017) 15162.
[29] J.W. Shin, S.H. Kwon, J.Y. Choi, J.I. Na, C.H. Huh, H.R. Choi, K.C. Park, Molecular mechanisms of dermal aging and antiaging approaches, Int. J. Mol. Sci. 20 (9) (2019).
[30] A. Desmoulière, A. Geinoz, F. Gabbiani, G. Gabbiani, Transforming growth factor-beta 1 induces alpha-smooth muscle actin expression in granulation tissue myofibroblasts and in quiescent and growing cultured fibroblasts, J. Cell Biol. 122 (1) (1993) 103–111.
[31] Y.Y. Wang, H. Jiang, J. Pan, X.R. Huang, Y.C. Wang, H.F. Huang, K.F. To, D. J. Nikolic-Paterson, H.Y. Lan, J.H. Chen, Macrophage-to-Myofibroblast transition

contributes to interstitial fibrosis in chronic renal allograft injury, J. Am. Soc. Nephrol. 28 (7) (2017) 2053–2067.
[32] K. Jinno, T. Takahashi, K. Tsuchida, E. Tanaka, K. Moriyama, Acceleration of palatal wound healing in Smad3-deficient mice, J. Dent. Res. 88 (8) (2009) 757–761.
[33] R. Yang, F. Liu, J. Wang, X. Chen, J. Xie, K. Xiong, Epidermal stem cells in wound healing and their clinical applications, Stem Cell Res. Ther. 10 (1) (2019) 229.
[34] C.L. Garcin, D.M. Ansell, The battle of the bulge: re-evaluating hair follicle stem cells in wound repair, Exp. Dermatol. 26 (2) (2017) 101–104.
[35] N. Ojeh, I. Pastar, M. Tomic-Canic, O. Stojadinovic, Stem cells in skin regeneration, wound healing, and their clinical applications, Int. J. Mol. Sci. 16 (10) (2015) 25476–25501.
[36] J.L. Spees, R.H. Lee, C.A. Gregory, Mechanisms of mesenchymal stem/stromal cell function, Stem Cell Res. Ther. 7 (1) (2016) 125.
[37] B. Calenic, M. Greabu, C. Caruntu, C. Tanase, M. Battino, Oral keratinocyte stem/progenitor cells: specific markers, molecular signaling pathways and potential uses, Periodontology 69 (1) (2000 2015) 68–82.
[38] J.L. Liesveld, N. Sharma, O.S. Aljitawi, Stem cell homing: from physiology to therapeutics, Stem Cell. 38 (10) (2020) 1241–1253.
[39] X.T. He, X. Li, Y. Xia, Y. Yin, R.X. Wu, H.H. Sun, F.M. Chen, Building capacity for macrophage modulation and stem cell recruitment in high-stiffness hydrogels for complex periodontal regeneration: experimental studies in vitro and in rats, Acta Biomater. 88 (2019) 162–180.
[40] J.J. Tomasek, G. Gabbiani, B. Hinz, C. Chaponnier, R.A. Brown, Myofibroblasts and mechano-regulation of connective tissue remodelling, Nat. Rev. Mol. Cell Biol. 3 (5) (2002) 349–363.
[41] J. Park, G. Yan, K.C. Kwon, M. Liu, P.A. Gonnella, S. Yang, H. Daniell, Oral delivery of novel human IGF-1 bioencapsulated in lettuce cells promotes musculoskeletal cell proliferation, differentiation and diabetic fracture healing, Biomaterials 233 (2020) 119591.
[42] D. Murugan Girija, M. Kalachaveedu, S. Ranga Rao, R. Subbarayan, Transdifferentiation of human gingival mesenchymal stem cells into functional keratinocytes by Acalypha indica in three-dimensional microenvironment, J. Cell. Physiol. 233 (11) (2018) 8450–8457.
[43] V. Bergoglio, F. Larcher, O. Chevallier-Lagente, A. Bernheim, O. Danos, A. Sarasin, M.D. Rio, T. Magnaldo, Safe selection of genetically manipulated human primary keratinocytes with very high growth potential using CD24, Mol. Ther. 15 (12) (2007) 2186–2193.
[44] S. Tancharoen, S. Gando, S. Binita, T. Nagasato, K. Kikuchi, Y. Nawa, P. Dararat, M. Yamamoto, S. Narkpinit, I. Maruyama, HMGB1 promotes intraoral palatal wound healing through RAGE-dependent mechanisms, Int. J. Mol. Sci. 17 (11) (2016).
[45] F.M. Ghazawi, J. Cyr, R. Darwich, M. Le, E. Rahme, L. Moreau, E. Netchiporouk, A. Zubarev, O. Roshdy, S.J. Glassman, D. Sasseville, I.V. Litvinov, Cutaneous malignant melanoma incidence and mortality trends in Canada: a comprehensive population-based study, J. Am. Acad. Dermatol. 80 (2) (2019) 448–459.
[46] P.A. Ascierto, R. Accorona, G. Botti, D. Farina, P. Fossati, G. Gatta, H. Gogas, D. Lombardi, R. Maroldi, P. Nicolai, M. Ravanelli, V. Vanella, Mucosal melanoma of the head and neck, Crit. Rev. Oncol. Hematol. 112 (2017) 136–152.
[47] F. López, J.P. Rodrigo, A. Cardesa, A. Triantafyllou, K.O. Devaney, W. M. Mendenhall, M. Haigentz Jr., P. Strojan, P.K. Pellitteri, C.R. Bradford, A. R. Shaha, J.L. Hunt, R. de Bree, R.P. Takes, A. Rinaldo, A. Ferlito, Update on primary head and neck mucosal melanoma, Head Neck 38 (1) (2016) 147–155.
[48] M. Mohammadi, M.R. Jaafari, H.R. Mirzaei, H. Mirzaei, Mesenchymal stem cell: a new horizon in cancer gene therapy, Cancer Gene Ther. 23 (9) (2016) 285–286.
[49] S. François, B. Usunier, M.E. Forgue-Lafitte, B. L'Homme, M. Benderitter, L. Douay, N.C. Gorin, A.K. Larsen, A. Chapel, Mesenchymal stem cell administration attenuates colon cancer progression by modulating the immune component within the colorectal tumor microenvironment, Stem Cells Transl. Med. 8 (3) (2019) 285–300.
[50] S. Guerrero, M. Inostroza-Riquelme, P. Contreras-Orellana, V. Diaz-Garcia, P. Lara, A. Vivanco-Palma, A. Cárdenas, V. Miranda, P. Robert, L. Leyton, M.J. Kogan, A.F. G. Quest, F. Oyarzun-Ampuero, Curcumin-loaded nanoemulsion: a new safe and effective formulation to prevent tumor reincidence and metastasis, Nanoscale 10 (47) (2018) 22612–22622.
[51] E.T. Firat, A. Dağ, A. Günay, B. Kaya, M. Karadede, B. Ersöz Kanay, A. Ketani, O. Evliyaoğlu, E. Uysal, The effect of low-level laser therapy on the healing of hard palate mucosa and the oxidative stress status of rats, J. Oral Pathol. Med. 43 (2) (2014) 103–110.
[52] G.F. Aiala, A.M. Oliveira, F.O. Costa, D.L. Fialho, A.S. Cunha Jr., P.A. Oliveira, Effect of local application of aminoguanidine on the biomechanical retention of implants in rats with induced diabetes, Int. J. Oral Maxillofac. Implants 28 (5) (2013) 1272–1277.
53 A.R. Farhad, S.M. Razavi, A.R. Rozati, N. Shekarchizade, M. Manshaei, Selective nitric oxide synthase inhibitor promotes bone healing, Dent. Res. J. 14 (5) (2017) 306–313.
[54] X. Wang, F. Lv, T. Li, Y. Han, Z. Yi, M. Liu, J. Chang, C. Wu, Electrospun micropatterned nanocomposites incorporated with Cu(2)S nanoflowers for skin tumor therapy and wound healing, ACS Nano 11 (11) (2017) 11337–11349.
[55] Ximu Zhang, Lin Jiang, Liwen Zheng, Ruyi Dang, Xiang Liu, Xiaoping Wang, Liling Chen, Yu Zhang Shrike, Jixi Zhang, Deqin Yang, A bioinspired hemostatic powder derived from the skin secretion of andrias davidianus for rapid hemostasis and intraoral wound healing, Small Nov (23) (2021), https://doi.org/10.1002/smll.202101699.
[56] Liwen Zheng, Qunhao Wang, Yu Zhang Shrike, Hongmei Zhang, yingying Tang, Yuxin Zhang, Wei Zhang, Ximu Zhang, A hemostatic sponge derived from skin secretion of Andrias davidianus and nanocellulose, Chem. Eng. J. 416 (2021).